Page Proof Instructions and Queries

Thank you for choosing to publish with us. This is your final opportunity to ensure your article will be accurate at publication. Please review your proof carefully and respond to the queries using the circled tools in the image below, which are available in Adobe Reader DC* by clicking **Tools** from the top menu, then clicking **Comment**.

Please use *only* the tools circled in the image, as edits via other tools/methods can be lost during file conversion. For comments, questions, or formatting requests, please use ⊤. Please do *not* use comment bubbles/sticky notes ✑.

*If you do not see these tools, please ensure you have opened this file with **Adobe Reader DC**, available for free at get.adobe.com/reader or by going to Help > Check for Updates within other versions of Reader. For more detailed instructions, please see us.sagepub.com/ReaderXProofs.

Sl. No.	Query
	Please note that we cannot add/amend orcid ids for any article at the proof stage. following orcid's guidelines, the publisher can include only orcid ids that the authors have specifically validated for each manuscript prior to official acceptance for publication.
	Please confirm that all author information, including names, affiliations, sequence, and contact details, is correct.
	Please review the entire document for typographical errors, mathematical errors, and any other necessary corrections; check headings, tables, and figures.
	Please ensure that you have obtained and enclosed all necessary permissions for the reproduction of art works (e.g. illustrations, photographs, charts, maps, other visual material, etc.) not owned by yourself. please refer to your publishing agreement for further information.
	Please note that this proof represents your final opportunity to review your article prior to publication, so please do send all of your changes now.
	Please confirm that the funding and conflict of interest statements are accurate.
1	Please Confirm that all Author Names are correct as set.
2	Please note that the bold text and sentences has made into normal text and sentences. Please check.
3	Please provide page number for Reference '1'.

Process and parameters for laser assisted localised heat treatment in manufacturing applications

Rui Pedro Pereira[1] (ID)**, Nuno Peixinho[1], Vitor Carneiro[1],**
Sara Cortez[1] (ID)**, Sérgio Luís Costa[2] and Vítor Blanco[2]**[AQ: 1]

Abstract

This paper presents information and results relevant for the development of a laser heat treatment process suitable to improve manufacturing in high strength steel and high strength aluminium alloys. The challenges with manufacturing of such materials include springback effect and localised fracture. The study details heat cycle and their effect in metallurgical state and mechanical properties. Such laser induced heat treatment process is intended to improve the forming behaviour of metal parts in challenging metal forming conditions, in particular for the delay or avoidance of localised fracture. Results for strength, hardness and elongation properties are presented. It was concluded that it is possible to locally modify yield strength and hardness using process duration suitable for industrial applications. Suitable process temperature ranges and target heat cycles were identified. A positive effect of material softening was observed in both hardness and strength properties. However, in some cases a reduction of ductility is apparent which must be considered for targeted industrial applications. The dimension of the heat-affected zone was also considered as design variable for the industrial process development. Preliminary results were obtained in a development forming tool.[AQ: 2]

Introduction

There is a dire need in the automotive sector to consider and develop cost and carbon footprint management tools and strategies for the survival of various manufacturing techniques.[1] Although weight saving is the key approach for reducing fuel consumption,[2] it also has adverse effects since safety may be compromised due to the employed thinner components.[3] To meet weight reduction concerns and safety in crashworthiness events, the use of high-strength steels (HSS) as well as aluminium alloys tends to increase because of their high specific strength.[4–6] However, these materials are characterised by their low formability at ambient temperatures,[7,8] and certain aspects such as wall thinning, springback and process parameters may lead to component failure[9–11] in deep-drawing processes. Tailor Heat Treated Blanks (THTB) feasibility to allow higher geometric complexity of metallic components has been investigated and corroborated. Due to a short-term laser heat treatment (LHT), localised material softening will allow for stress redistribution during

the forming process that if executed in adequate areas reduce the risk of failure.[12] The adapted pattern of soft and strength areas along the blank facilitates both material flow and local forming forces during the forming operation to be influenced. While for AA6XXX, LHT is never applied directly in critical areas but only to adjoining zones, hence lower stresses in the critical force transferring areas will occur.[13] For HSS as ductility is positively affected,[14–16] the key idea is to LHT regions where high deformation degrees are needed.[7]

Authors have confirmed the formability increase of aluminium alloys series 6XXX made out of THTB.[17–19] Piccininni and Palumbo[17] have confirmed an improvement of AA6082-T6 material drawability of a circular

[1]University of Minho, Braga, Portugal
[2]Bairrimoldes LDA, Anadia, Portugal

Corresponding author:
Rui Pedro Pereira, University of Minho, Campus de Azurém, Av. da Universidade, Guimarães, Braga 4800-058, Portugal.
Email: a81833@alunos.uminho.pt

cup geometry up to 22%. Geiger et al.[13] have achieved a maximum drawing depth increase of about 86% of a more complex drawing part made out of AA6181-T4. Implementation of THTB in the hydromechanical deep-drawing process[18] and multi-layered, ultra-fine sheet material of AA6014-T4 was also effective.[20] The feasibility of material softening was also investigated in 2XXX aluminium alloy series. Mohammadi et al.[21] conducted flexural tests having found that the elastic return can be reduced by 43% in AA2024-T3. A mock-up geometry made of martensitic steel revealed a significant decrease of 78% of the sliding force.[7]

Merklein et al.[22] have identified four parameters, regarding the temperature – time profile, as the most important for the manufacturing of THTB: (1) heating rate; (2) holding time; (3) cooling time and (4) maximum temperature. Meanwhile, the heating technology must comply with three key requirements as stated by Merklein et al.[23]: high heating rate; temperature uniformity; and third, reproductivity of the heating parameters.

Concerning heat treatment conducted in aluminium alloys, the three first parameters named have been seen as important to confine the heat-affected zone (HAZ). The natural cooling enhanced a sharp transition and thus, a separation between the heat-treated and non-heat-treated areas.[22] As for the maximum temperature, Geiger et al.[13] specified that all relevant microstructural mechanisms in the context of THTB directly correlate with the maximum temperature; indeed, most of the authors correlate material softening as a function of the LHT maximum temperature.[24,25] Regarding HSS, there is still a lack of experimental data to determine maximum temperature influence. Lapouge et al.[15] did a comprehensive material characterisation of the softening mechanisms for DP 1180 and MS1500 for a wide range of maximum temperatures. The aim was to correlate the microstructural modifications, hence mechanical resistance as a function of austenisation critical temperatures. Previously, Capello and Previtali[14] did compare a tempering and annealing local laser heat treatment. In their targeted softening effects both heating and cooling time changed between each temperature.

A 6000 series alloys gain the majority of their strength through a fine distribution of strengthening particles which can be precipitated with a dedicated heat treatment.[26] These precipitates occur in several forms which can be divided into three categories: (1) coherent β'', (2) partially coherent β' and (3) incoherent β.[27] Through a Differential Scanning Calorimetry (DSC) analysis the phenomenology of precipitation mechanisms can be studied.[28–32] DSC analysis is useful to study the underlying influence of the heating rate on the precipitation mechanism. Osten et al.[32] research was decisive in creating continuous heating dissolution (CHD) diagrams evaluating the effect of both maximum temperature and heating rate. Based on their work, Fröck et al.[33] anticipated the optimal maximum temperatures of local laser heat treatment leading to AA6060-T4 softening.

As far as dual-phase steel concerns, they are characterised by a hard martensitic phase dispersed within a soft ferrite matrix.[34] Within the scope of a short-term local LHT two softening mechanisms can be pursued: (1) tempering of martensite, for maximum heating temperature below T_{Ac1}, which leads to a sufficient softening of the initial microstructure and (2) martensite transformation into austenite during heating and austenite transformation into ferrite during cooling, for maximum heating temperature higher than T_{Ac1}.[35] In order to optimise heat treatment process window, continuous cooling transformation (CCT) diagrams are used, as they provide information on the microconstituents formed from the non-isothermal austenite decomposition.[36]

This paper is aimed at studying local short-term LHT for improvement of cold work forming processes formability. Maximum temperature is considered the most important variable to trigger softening mechanisms. However, heat and/or cooling rate may be considered as they influence not only optimal maximum temperature for softening achievement, but also mechanical properties modification. To study the influence of heating rate on microstructural evolution of AA6063-T6 a calorimetry analysis is performed. The CCT diagram allowed predicting the influence of the cooling rate for phase transformation of DP 1000 steel. Finally, experimental results reveal improved performance for locally laser heat treated prototypes of DP 1000.

Materials and methods

Materials

In this study, two different materials were examined. The first to consider is a 6000 series aluminium, AA6063-T6, having a sheet thickness of 2 mm. The second is a DP 1000 steel consisting of a ferritic/martensitic structure with a sheet thickness of 1 mm.

Table 1 presents the chemical composition that was obtained from a 'Phillips X'Unique II' spectrometer. Critical temperatures for phase transformation (T_{Ac1} and T_{Ac3}) and the start temperature of martensite transformation (T_{Ms}) were calculated based on a 0.2% carbon steel using empirical formulas for DP steel.[37,38] Quasi-static mechanical properties are summarised in Table 2.

Local laser heat treatments

The laser equipment used and processing parameters are different for the two studied materials.

The experimental procedure is temperature controllable by a non-contact pyrometer, which is used as the main information source for the laser power control algorithm for both materials tested. Figure 1 presents

Table 1. Chemical composition of the tested alloys (wt%).

	Al	Si	Ti	V		Mn	Fe
6063-T6	98.650	1.112	0.013	0.013		0.017	0.187
	Fe	C	Mn	Si	Cr	Ni	Co
DP 1000	95.790	0.080	2.900	0.620	0.350	0.160	0.100

Table 2. Mechanical properties of the tested alloys.

	Hardness HV	$Rp_{0.2}$ (MPa)	UTS (MPa)	Elongation (%)
6063-T6	95	237.4	265.6	8.5
DP 1000	345	706.0	1075.7	10.8

the laser equipment. Due to distortion driven by large heat-affected zone, the DP steel had to be clamped.

Regarding aluminium alloy, local laser heat treatment was performed using a 'Mergenthaler LM100' laser equipment. The selected focus region was a $10 \times 10\,mm^2$, $20 \times 10\,mm^2$ and $60 \times 10\,mm^2$ area that is highlighted in the specimen design presented in Figure 2, depending on the strategy applied. For strategy one, the cylindrical laser beam has suffered no movement. On the other hand, strategies two and three had a constant linear speed of 1 mm/s. Laser beam diameter remained invariable, assuming the value of 10 mm.

With respect to DP 1000, laser treatments were conducted with diode laser equipment on a rectangular sample measuring $250 \times 120 \times 1\,mm^3$. The laser spot has a rectangular shape of 5.5 mm in length. Laser beam width assumes the value of 20 or 30 mm. Movement of the heat source travelled the entire sheet from one edge to the opposite, after which dog-bone specimens were cut.

Experimental formability tests

A progressive tooling system was developed for cold forming of blanks with sheet thickness not exceeding 1 mm. Due to the availability of thin sheets, forming tests were performed on DP 1000 prototypes. The experimental procedure is divided into two forming operations: (1) Deep-drawing of a Circular Cup; (2) Local Bending Operation. Local laser heat treatment is performed prior to any forming operation, as suggested in Figure 3, which also illustrates geometry configuration after each forming operation.

The purpose of the experimental two-step forming operation is to increase geometric aggressiveness in order to accentuate localised failure problems and, consequently, to have a more convergent failure analysis with the potential difference and comparison with local laser heat-treated layouts. The four tested models and laser heat treatment conditions are presented in Table 3.

DSC analysis

DSC analysis was performed on a 'DSC Q20' equipment and was carried out in AA6063-T6 in its initial state prior to any laser heat treatment. The sample was heated from RT up to 400°C, the heating rate was small to make possible individualisation of endothermic/exothermic peaks, assuming the value of 0.09 K/s in an argon atmosphere (50 mL/min). Pure aluminium was the reference material and the mass of the sample was 13 mg.

The original DSC curve obtained is presented in Figure 4(a). The first step was the baseline-subtraction represented by a polynomial function. The curve was normalised by dividing the mass of the test sample. Handling of data was done via specific heat capacity
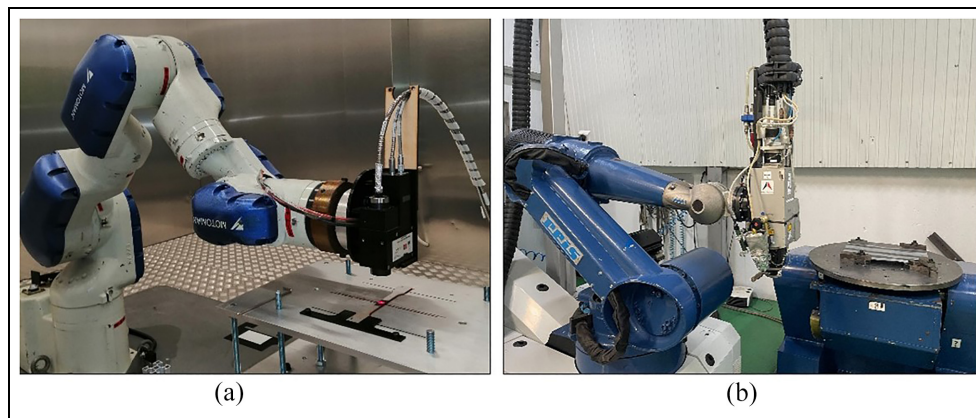
Figure 1. Specimen fixture and laser head applied on: (a) AA6063-T6 and (b) DP 1000.
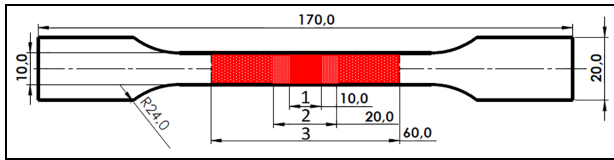
Figure 2. Specimen design and laser focus area dimensions for each heat treatment strategy applied.

- Three endothermic peaks, named B, F and H at 203°C, 291°C and 386°C, respectively;
- Two exothermic peaks, named *d* and *g*, at 255°C and 352°C, respectively.

$$c_p = \frac{\dot{Q}_{sample} - \dot{Q}_{baseline}}{m.\beta} \tag{1}$$

(Figure 4(b)) so that dissolution/precipitation mechanisms could be identified and analysed. To do so equation (1) was applied.

Hardness and uniaxial tensile tests

Vickers indenter on a 'Galileo D200' durometer was used. The measurement points include the laser focus zone in the incident and opposite surface of the specimens. The heat-affected zone was analysed by extending hardness measurement points along the longitudinal axis of the specimen. Quasi-static mechanical properties were obtained following EN 10002-1 standard using a universal tensile testing machine (Instron, 25 kN). The tensile yield strength at 0.2 % offset (Rp0.2), Ultimate Tensile Strength (UTS) and elongation at fracture for an initial gauge length of 60 mm (AA6063-T6) and 80 mm (DP 1000) were calculated. Tensile tests were performed 24 h after local laser heat treatment.

Process window for softening mechanisms activation

Precipitation sequence and aging behaviour of AA6063-T6

For a slow heating rate of 0.09 K/s, five exothermic/endothermic peaks can be spotted in Figure 4(b), as follows:

As expected, the first peak observed corresponds to an endothermic reaction, as a consequence of both GP-zones and β'' have been previously precipitated in T6 condition. The authors's research is not consensual about peak d precipitation reaction identification. Some authors, such as Osten et al.[32] state that the first exothermic peak observed corresponds to the β' phase precipitation. On the other hand, Liu et al.[30] identified the same reaction as the β'' phase precipitation, since it is considered that the first endothermic reaction only corresponds to the dissolution of GP-zones. Table 4 summarises the approach followed by both authors.

Based on the research developed by Osten et al.[32] continuous heating dissolution (CHD) diagrams are used to optimise heat treatment shops, since higher heating rates shift precipitation/dissolution reaction towards higher temperatures. Therefore, the identification of precipitation and dissolution reactions, as a function of maximum temperature and heating rate can be estimated by the support of CHD diagrams.

According to Figure 5, for heating rates between 10 and 40 K/s process window, that is, maximum temperature for material softening achievement. Reaction F is chosen due to a more significant potential for material softening, corresponding to a range of temperature from 357°C up to 459°C at which complete dissolution of β'' and GP-Zones is predictably achieved. Details for precipitation/dissolution tendency lines extrapolation are given by Osten et al.[32] since AA6016-T6 has a similar mass fraction of Mg and Si of the investigated alloy.
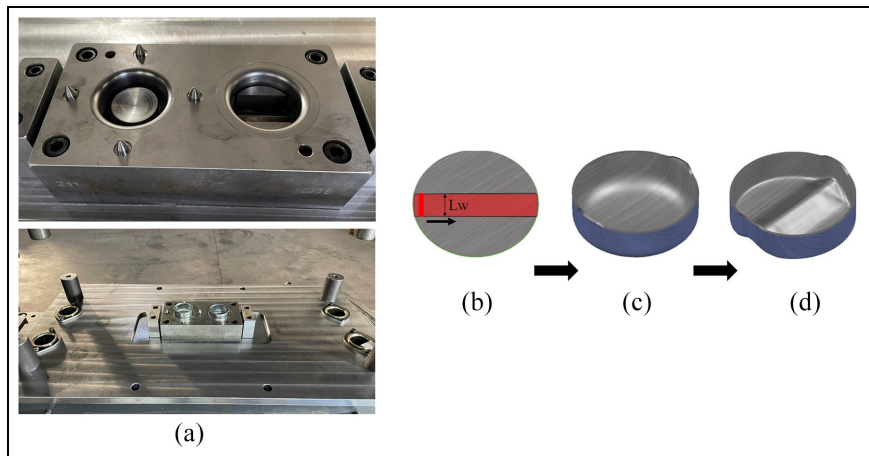

Figure 3. Formability tests: (a) tool elements, (b) tailor heat treated blank, (c) component after first forming operation and (d) component after second forming operation.

Table 3. Heat treated and base material layouts.

Layout	$T_{max}(°C)$	Laser beam width, L_w [mm]	Cooling rate [K/s]	
			Formula[39]	Numerical model
(1)	Base material			
(2)	600	30	23.2	22.1
(3)	600	20	34.0	37.7
(4)	800	30	38.8	37.1

Influence of process parameters on the temperature – Time curve of DP1000

The cooling rate plays a key role in the final microstructure formed, as it influences the volume fraction of the martensitic/ferritic phase. Cooling is determined by thermal conduction with the surrounding material, so as by the thermal interaction between sample surfaces and the environment: radiation and convection.

Figure 6 presents a simplified model of the local laser heat treatment applied to the steel sheet sample.

The application of the analytical model is summarised as follows and it was developed by Bergweiler[39] The assumption of homogeneous temperature distribution of the laser beam is considered.

According to the Fourier First law, heat flux through conduction in a rectangular slab is:

$$\dot{Q}_{cond.} = \dot{q}_{cond.}.d_p.2.(S_L + L_w) \tag{2}$$

As a consequence of thermal agitation, heat transfer through radiation takes place. At the same time, laser beam energy generates mass motion of air. Hence, convective and radiative heat transfer can be determined:

$$\dot{Q}_{\substack{rad. \\ conv.}} = (\dot{q}_{rad.} + \dot{q}_{conv.}).2.S_L.L_w \tag{3}$$

Therefore, cooling rate can be determined by the following expression:

$$\frac{dT}{dt} = \frac{2.\dot{q}_{cond.}}{L_w.\rho.c_p} + \frac{2.(\dot{q}_{rad.} + \dot{q}_{conv.})}{d_p.\rho.c_p} \tag{4}$$

The numerical model was conducted in *Ansys Workbench*. The blank was meshed with 13,000 linear hexahedral elements. Modelling of laser heating was
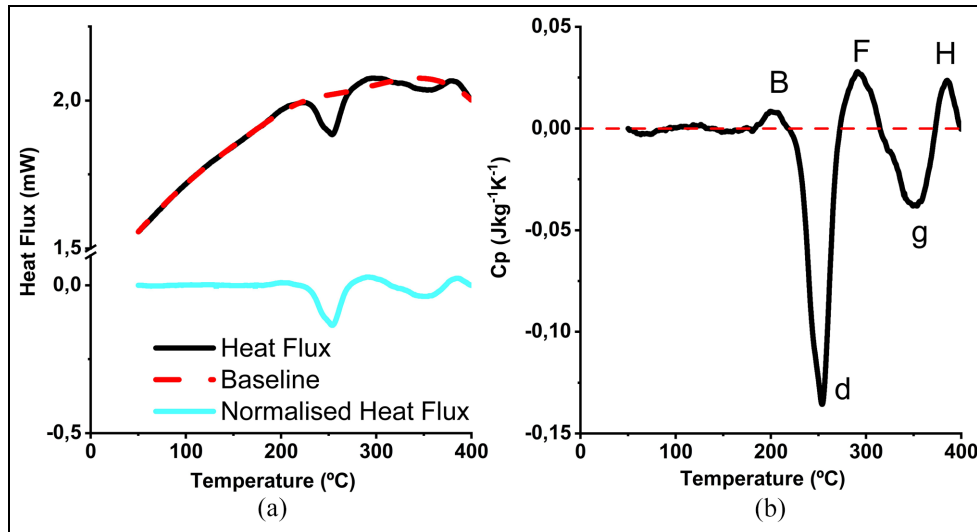

Figure 4. AA6063-T6 DSC measurements: (a) data handling to obtain normalised DSC heating curve and (b) specific heat capacity curve for a heating rate of 0.09 K/s.

Table 4. Microstructural kinematics evolution based on DSC measurements based on two different al. alloys.

Peak	Reaction	Mechanism, according to:	
		AA6005-T6 (SAn[a] + WQ + AA)[32]	AA6013-T6 (SST + WQ + SA[b])[30]
B	Endothermic	GP-zones and β'' dissolution	GP-zones dissolution
d	Exothermic	β' precipitation	β'' precipitation
F	Endothermic	β' dissolution	β'' dissolution
g	Exothermic	β precipitation	β' precipitation
H	Endothermic	All precursor phases dissolution	β' dissolution

[a]Solution Annealing 540°C/20 min.
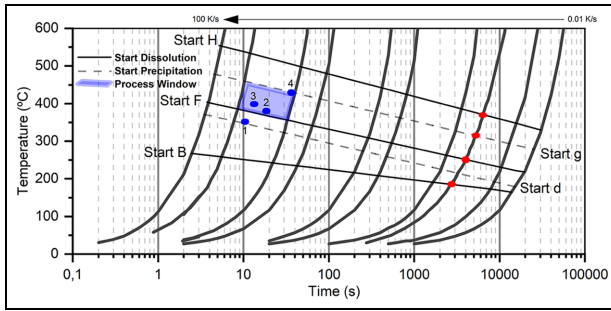[b]Static aged at 191°C.

Figure 5. CHD diagram and identification of process window for aluminium alloy 6063-T6 (based on the work developed by Osten et al.[32]).

performed using a movable heat flux with a scanning speed of 8.3 mm/s. Both sides of the sheet are subjected to convection, and radiation losses were also considered. The absorption coefficient assumes the constant value of 0.55 in this model. The temperature during treatment is modelled with the set of parameters listed in Table 5. The numerically predicted cooling rate presents values very close to those obtained through equation (4) as shown in Table 3.

Formula (4) presents useful information regarding the influence of beam size on heat treated area cooling rate:

- The higher the laser beam width the slower the cooling rate;
- As for the length of laser beam focus, no direct influence on cooling rate is considered.
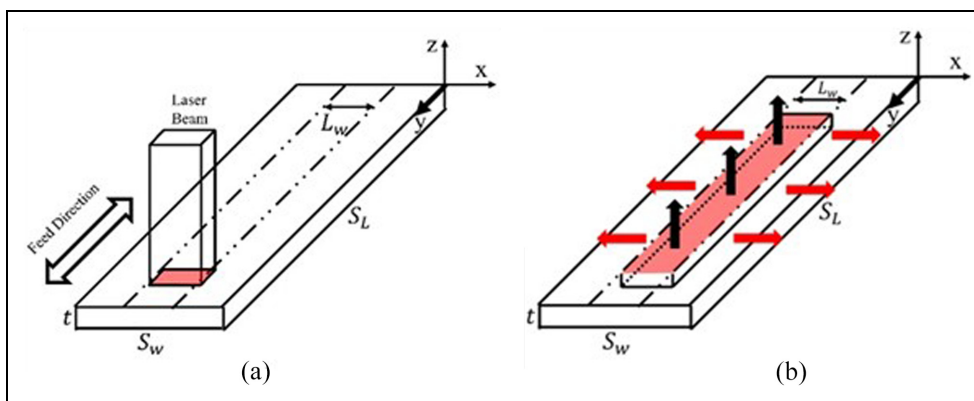
Based on the analytical thermal model, different temperature profiles can be depicted on the continuous cooling transformation diagram. Figure 7 presents three different temperature profiles, which can be representative of the microstructural evolution of the steel during cooling. Two softening mechanisms can be identified:

- At a peak temperature of 600°C, $T_{Ms} < T_{max} < T_{Ac1}$, tempering of martensite is expected.[35] An increasing laser beam focus width has a neglected effect on the final formed microstructure;
- At a peak temperature of 800°C, $T_{Ac1} < T_{max} < T_{Ac3}$ or $T_{max} > T_{Ac3}$, the cooling rate has a strong influence on the desired microstructure evolution. The slower the cooling rate, the more volume fraction of ferrite is formed during cooling at the expense of martensite volume fraction reduction.

Materials characterization: Results and discussion

Mechanical properties modification as a function of laser heat treatment maximum temperature is summarised in Figure 8 for the two investigated materials. Hardness (Figure 8(a)–(c)), as well as yield stress, ultimate tensile stress and elongation at fracture evolution (Figure 8(c) and (d)), allowed the identification of suitable maximum temperatures for material softening achievement.
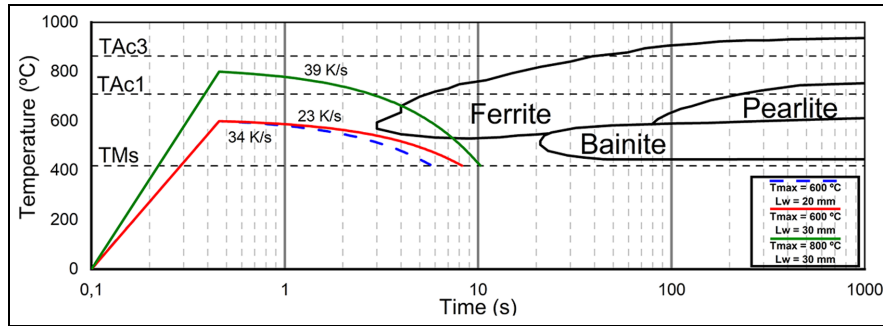

Figure 6. Schematic representation of: (a) laser beam feed direction and (b) heat transfer through conduction, convection and radiation.

Table 5. Parameters used in the modelling of laser heat treatment (based on refs.[14,15]).

	$\lambda(W.m^{-1}.K^{-1})$	$c_p(J.kg^{-1}.K^{-1})$	$\alpha(W.m^{-2}.K^{-1})$	$\rho(kg.m^{-3})$	$T_0(K)$
DP1000	28	560	20	7860	293.15

Figure 7. Analytical prediction of temperature – time profile of DP 1000 in a reference point of heat-affected zone and indicative CCT diagram (adapted from[14]).
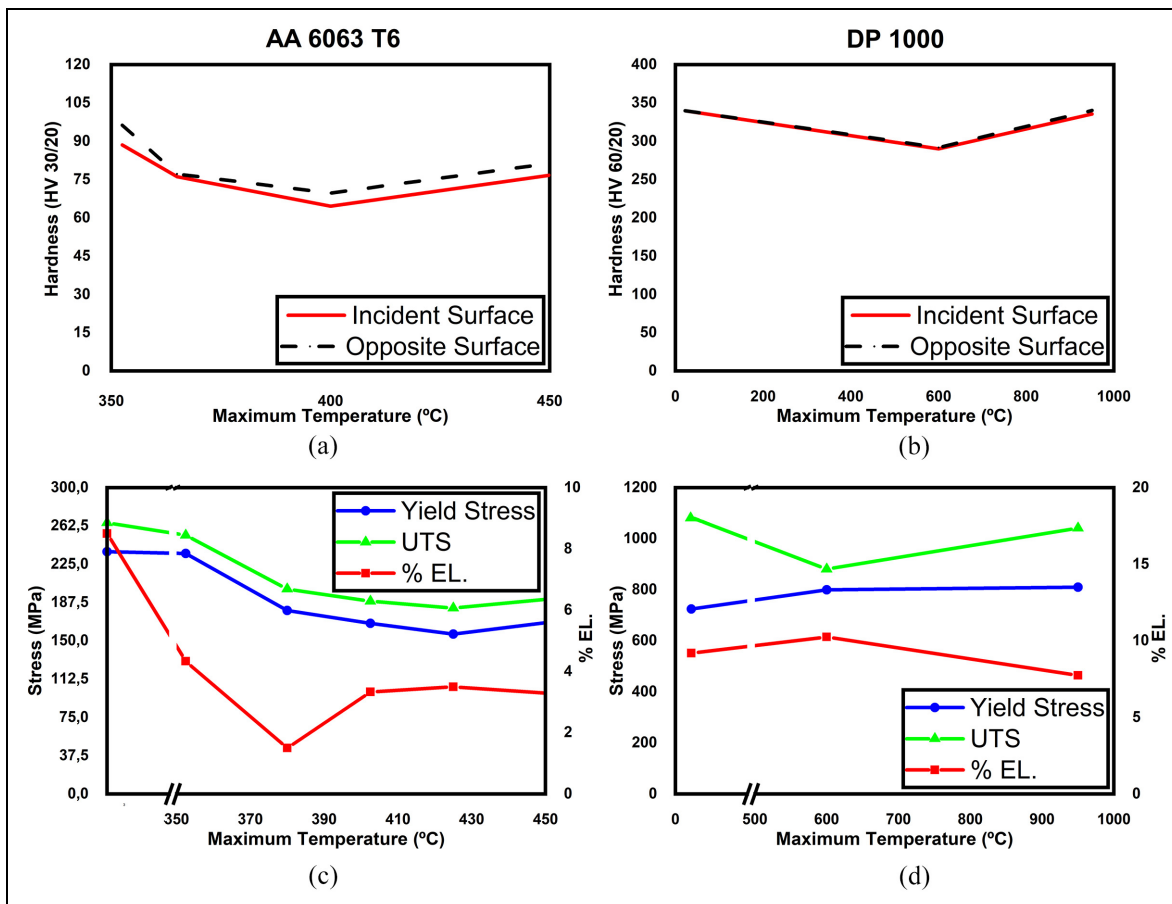

Figure 8. Mechanical properties modification as a function of maximum temperature for the two studied materials: (a and b) hardness fluctuation and (c and d) yield stress, UTS and %EL.

Aluminium alloy AA6063-T6

The analysis of hardness results allowed for the identification of suitable heat treatment temperatures in the range of 365 – 450°C, that were capable of providing a significant reduction in hardness. According to Figure 8(a) it can be observed that the maximum hardness reduction of 32% occurs at a selected maximum temperature of 400°C. Instead, at 353°C the hardness reduction is insignificant.

From Figure 8(c) a material softening is observed at the range of maximum temperature of 380°C – 455°C. The maximum softening is reached at 425°C corresponding to a Yield and UTS decrease of 34% and 31%, respectively. However, local laser heat treatment influence is also observed in the elongation at fracture.

As the maximum hardness reduction occurred at 400°C, Figure 9(a) to (c) presents the hardness evolution along the specimen according to the strategy applied, for this peak temperature. The average hardness value for the HAZ of $60 \times 10\,\text{mm}^2$ at the incident and opposite surface assumes the value of 73 ± 1.6 and
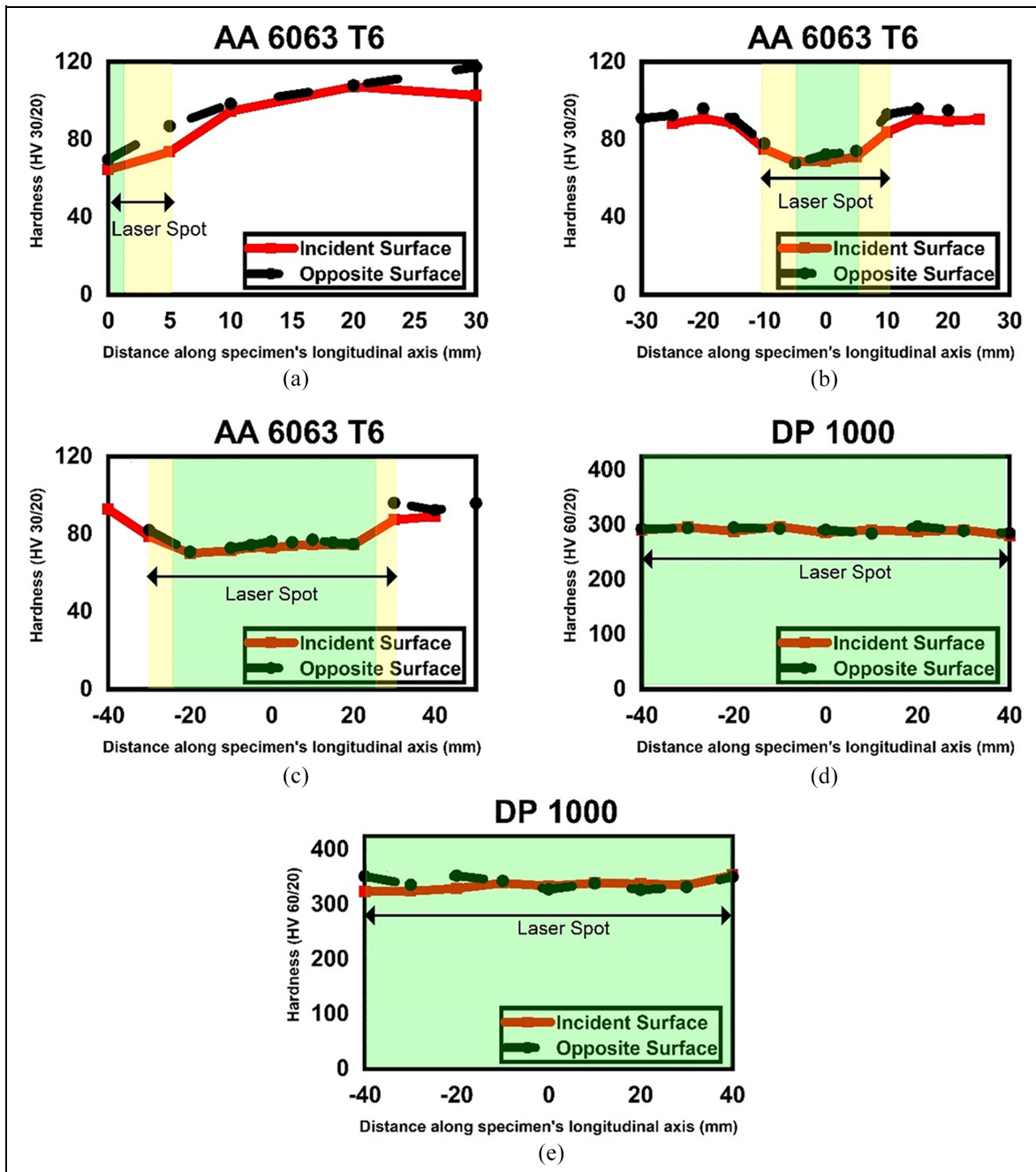
Figure 9. Variation of hardness along specimen's longitudinal axis. Origin set at specimen's geometric centre: (a) $T_{max} = 400°C$, HAZ $= 10 \times 10$ mm^2; (b) $T_{max} = 400°C$, HAZ $= 20 \times 10$ mm^2; (c) $T_{max} = 400°C$, HAZ $= 60 \times 10$ mm^2; (d) $T_{max} = 600°C$, $L_w = 20$ mm; (e) $T_{max} = 950°C$, $L_w = 20$ mm.

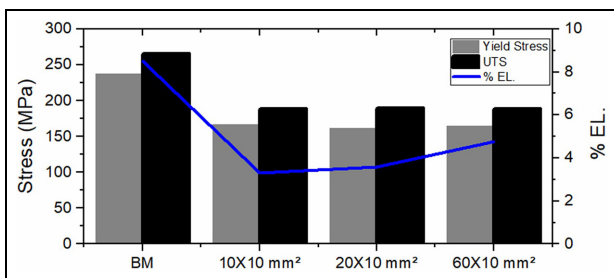**Figure 10.** Evolution of mechanical properties according to the increased HAZ for a maximum temperature of 400°C.

74.8 ± 1.9 HV respectively, showing that the temperature uniformity along HAZ is successfully achieved.

Because of the drastic decrease in the elongation at fracture, results depicted in Figure 10 suggest that an increase in the HAZ enables recovery of the ductility at a peak temperature of 400°C. Alongside, only a small variation in mechanical resistance is observed: yield and ultimate tensile stress assume the value of 1645 ± 7 and 1890 ± 8 MPa, respectively. This is important for material characterisation as with only a small portion of the tensile specimen heat treated, mechanical properties

Table 6. Correlation between both maximum temperature and heating rate with material softening.

Code (in Figure 5)	Maximum temperature [°C]	Predominant reaction	$\Delta\sigma_u$ (%)
I	350	Precipitation	−5
2	380	Dissolution	−24
3	400		−29
4	425		−3I

modification can be adequately estimated. However, the closer the elongation at fracture is to its initial values with increasing HAZ. Thus, for material characterisation purposes the local laser heat treatment should be executed to the entire blank, after which the specimen should be cut.

The prediction of the CHD diagram for high heating rates, and consequently the precipitation and dissolution phenomena correlate with the tensile test results as shown by the reference point illustrated in Figure 5 and Table 6. For a peak temperature/heating rate located where a precipitation mechanism takes place, softening of material is quite low. As the dissolution of β'' and/or β' becomes prevalent, the material's softening is achieved. Mechanical resistance softening is first observed at 380°C, reaching maximum softening at 425°C where endothermic reaction F is completed.

DP 1000 steel

No improvement in material softening by laser heat treatment at a maximum temperature of 950°C is observed. On the other hand, at a maximum temperature of 600°C hardness and UTS reduction of 13 % (Figure 8(b)) and 19% (Figure 8(d)) are noticed, respectively.

The hardness fluctuation results along the laser beam scan for the DP 1000 investigated steel are presented in Figure 9(d) and (e). The proximity of values between both surfaces allows us to infer that the laser radiation affected both surfaces of the material almost equally throughout the scan. The laser radiation was effective in homogeneously softening the mechanical strength of the material, both in the feeding direction and in its thickness.

Different softening mechanisms, activated accordingly to the selected maximum temperature, result in diverging mechanical properties modifications. Tempering of martensite takes place for a maximum temperature in the range of $T_{Ms} < T_{max} < T_{Ac1}$. Hence, material softening is observed at 600°C. Ferrite aging does not affect ductility, in fact, a small increase in elongation at fracture is noticed. As a negative effect, a strain hardening decrease of 70 % may compromise the potential of material softening due to local laser heat treatment for this tested temperature in sheet metal forming applications.

Experimental metal forming tests for DP 1000 steel

After the first forming operation no evidence of fracture is detected, independently of the evaluated models. According to experimental results after the second forming operation presented in Figure 11, the three laser heat-treated layouts reveal improved results in comparison with the base material layout. Model 4 reveals the most significant degree of improvement achieved among the models tested herein, both qualitatively and quantitatively, in the characterisation of severe rupture of the proposed models. The fracture area, F_A, of the model with a maximum temperature of 800°C and laser beam width of 30 mm is 89% less than the base material fracture area. Moreover, a maximum temperature of 600°C, $T_{Ms} < T_{max} < T_{Ac1}$, no influence of laser beam width and thus cooling rate is noticed as the fracture area of both layouts 2 and 3 practically assumes the same value, even if the analytically/numerically predicted cooling rate is higher for layout three (34 K/s) compared to layout two (23 K/s). The extreme conditions in the test geometry had the desired effect in the search for a destructive model that evidenced identifiable and convergent conditions in the comparative analysis.

Conclusions

The potentiality of THTB to reduce the risk of fracture of manufactured prototypes and components has been

$F_A = 163\ mm^2$ $F_A = 47\ mm^2$ $F_A = 51\ mm^2$ $F_A = 18\ mm^2$
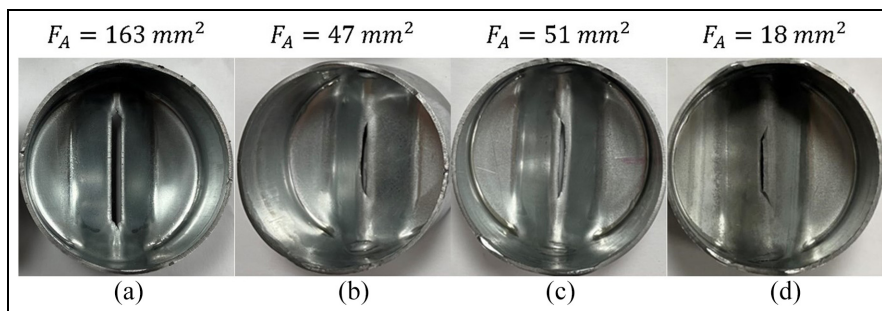
(a)   (b)   (c)   (d)

Figure 11. Representative prototypes - comparison between the four evaluated models: (a) Layout 1; (b) Layout 2; (c) Layout 3; and (d) Layout 4.

demonstrated by other authors. In this paper, microstructural mechanisms activation for material's softening was studied based on temperature – time profile in a short-term local laser heat treatment.

Regarding aluminium alloy, the microstructural evolution is mainly correlated with the maximum temperature. In this paper, based on the continuous dissolution diagram, the influence of the heating rate on precipitation/dissolution phenomena was incorporated. The tensile tests results correlate well with the influence of maximum temperature and heating rate on microstructure evolution: localised heat treatment via laser radiation at maximum heating rates and temperatures situated in dissolution reactions had as a consequence a substantial reduction of the ultimate tensile strength, this reduction being more significant the closer to the end of the dissolution reaction. On the other hand, at the temperature and heating rate tested in the range of occurrence of particle precipitation phenomena, the softening of the material was insignificant. This is of vital importance as the genesis of THTB demands the knowledge of underlying mechanisms which govern the strengthening/softening phenomenon. As for DP 1000, the perpendicular direction of the laser beam about the feeding rate can be manipulated for cooling rate control.

Preliminary experimental tests on a validation geometry yielded improved performance for the layouts with modifying pattern of mechanical properties. Even though, the component could not be successfully produced without cracking due to the severity of the second forming operation, a considerable improvement both qualitatively and quantitatively of laser heat-treated models is noticed.

Declaration of conflicting interests

The author(s) declared no potential conflicts of interest with respect to the research, authorship, and/or publication of this article.

Funding

ORCID iDs

Rui Pedro Pereira (ID) https://orcid.org/0000-0003-4630-3843
Sara Cortez (ID) https://orcid.org/0000-0002-2794-084X

References

1. Riaz AA, Hussain G, Iqbal A, et al. Energy consumption, carbon emissions, product cost, and process time in incremental sheet forming process: A holistic review from sustainability perspective. *Proc IMechE, Part B: J Engineering Manufacture* 2022; 236(13).[AQ: 3]

2. Aminzadeh A, Parvizi A, Safdarian R, et al. Comparison between laser beam and gas tungsten arc tailored welded blanks via deep drawing. *Proc IMechE, Part B: J Engineering Manufacture* 2021, 235(4): 673–688.

3. Mori KI and Abe Y. A review on mechanical joining of aluminium and high strength steel sheets by plastic deformation. *Int J Lightweight Mater Manuf* 2018; 1(1): 1–11.

4. Abe Y, Saito T, Mori KI, et al. Mechanical clinching with dies for control of metal flow of ultra-high-strength steel and high-strength steel sheets. *Proc IMechE, Part B: J Engineering Manufacture* 2018; 232(4): 644–649.

5. Pham TH, Nguyen DT, Banh TL, et al. Experimental study on the chip morphology, tool-chip contact length, workpiece vibration, and surface roughness during high-speed face milling of AA6061 aluminum alloy. *Proc IMechE, Part B: J Engineering Manufacture* 2020; 234(3): 610–620.

6. Peixinho N, Jones N and Pinho A. Application of dual-phase and TRIP steels on the improvement of crashworthy structures. *Mater Sci Forum* 2005, 502: 181–188.

7. Neugbauer R, Scheffler S, Poprawe R, et al. Local laser heat treatment of ultra high strength steels to improve formability. *Prod Eng Res Devel* 2009; 3: 347–351.

8. Machhammer M and Sommitsch C. The interaction between short-term heat-treatment and the formability of an Al-Mg-Si alloy regarding deep drawing processes. *IOP Conf Ser Mater Sci Eng* 2016; 159: 012001.

9. Atul ST and Babu MCL. A review on effect of thinning, wrinkling and spring-back on deep drawing process. *Proc IMechE, Part B: J Engineering Manufacture* 2019; 233(4): 1011–1036.

10. Lajarin SF and Marcondes PVP. Influence of process and tool parameters on springback of high-strength steels. *Proc IMechE, Part B: J Engineering Manufacture* 2015; 229(2): 295–305.

11. Filho RAC, Triguinho LMV, Neto RCB, et al. An experimental approach for blankholder force determination for DP600 with different material flow strain rates in the flange during stamping. *Proc IMechE, Part B: J Engineering Manufacture* 2013; 227(3): 417–422.

12. Peixinho N, Pereira R, Carneiro V, et al. Development of laser heat treatment process for assisted forming of aluminum alloys. In: *2021 6th International Conference on Smart and Sustainable Technologies (SpliTech)*, Split, Croatia, 8–11 September 2021. New York: IEEE.

13. Geiger M, Merklein M and Vogt U. Aluminum tailored heat treated blanks. *Prod Eng* 2009; 3: 401–410.

14. Capello E and Previtali B. Enhancing dual phase steel formability by diode laser heat treatment. *J Laser Appl* 2009; 21: 1–9.

15. Lapouge P, Dirrenberger J, Coste F, et al. Laser heat treatment of martensitic steel and dual-phase steel with high martensite content. *Mater Sci Eng: A* 2019; 752: 128–135.

16. Järvenpää A, Jaskari M, Hietala M, et al. Local laser heat treatments of steel sheets. *Phys Procedia* 2015; 78: 296–304.

17. Piccininni A and Palumbo G. Design and optimization of the local laser treatment to improve the formability of age hardenable aluminium alloys. *Materials* 2020; 13(7): 1–22.

18. Piccininni A, Di Michele G, Palumbo G, et al. Improving the hydromechanical deep-drawing process using aluminum tailored heat treated blanks. *Acta Metall Sin Engl* 2015; 28(12): 1482–1489.

19. Merklein M, Böhm W and Lechner M. Tailoring material properties of aluminum by local laser heat treatment. *Phys Procedia* 2012; 39: 232–239.

20. Herrmann J and Merklein M. Improvement of deep drawability of ultra-fine grained 6000 series aluminum alloy by tailored heat treatment. *Procedia Manuf* 2018; 15: 976–983.

21. Mohammadi A, Vanhove H, Van Bael A, et al. Bending properties of locally laser heat treated AA2024-T3 aluminium alloy. *Phys Procedia* 2012; 39: 257–264.

22. Merklein M and Nguyen H. Advanced laser heat treatment with respect for the application for tailored heat treated blanks. *Phys Procedia* 2010; 5: 233–242.

23. Merklein M, Geiger M, Staud D, et al. Tailored heat treated blanks applied on car body parts under quasi-series conditions. *Int J Microstruct Mater Prop* 2009; 4(5/6): 525–533.

24. Lattanzi A, Piccininni A, Guglielmi P, et al. A fast methodology for the accurate characterization and simulation of laser heat treated blanks. *Int J Mech Sci* 2021; 192(2): 10613.

25. Geiger M, Merklein M and Kerausch M. Finite element simulation of deep drawing of tailored heat treated blanks. *CIRP Ann Manuf Technol* 2004; 53(1): 223–226.

26. Poznak A, Thole V and Sanders PG. The natural aging effect on hardenability in Al-Mg-Si complex interaction between composition and heat treatment parameters. *Metals* 2018; 8(5): 309–332.

27. Chauhan KPS. Influence of heat treatment on the mechanical properties of aluminium alloys (6xxx series): a literature review. *Int J Eng Res* 2017; V6(3): 386–389.

28. Miao WF and Laughlin DE. A differential scanning calorimetry study of aluminum alloy 6111 with different pre-aging treatments. *J Mater Sci Lett* 2000; 19(3): 201–203.

29. Chen Z, Liu K, Elgallad E, et al. Differential scanning calorimetry fingerprints of various heat-treatment tempers of different aluminum alloys. *Metals* 2020; 10(6): 763–779.

30. Liu M, Wu Z, Yang R, et al. DSC analysis of static and dynamic precipitation of an Al-Mg-Si-Cu aluminum alloy. *Prog Nat Sci Mater Int* 2015; 25(2): 153–158.

31. Chang CST and Banhart J. Low-temperature differential scanning calorimetry of a Al-Mg-Si alloy. *Metall Mater Trans A Phys Metall Mater Sci* 2011; 42(7): 1960–1964.

32. Osten J, Milkereit B, Schick C, et al. Dissolution and precipitation behaviour during continuous heating of Al-Mg-Si alloys in a wide range of heating rates. *Materials* 2015; 8(5): 2830–2848.

33. Fröck H, Graser M, Milkereit B, et al. Precipitation behaviour and mechanical properties during short-term heat treatment for tailor heat treated profiles (THTP) of aluminium alloy 6060 T4. *Mater Sci Forum* 2016; 877: 400–406.

34. Bandyopadhyay K, Panda SK and Saha P. Prediction of formability of laser-welded dual-phase steel by finite element analysis. *Proc IMechE, Part B: J Engineering Manufacture* 2014; 228(9): 1048–1057.

35. Carlsson C. Local heat treatment of ultra high-strength-steel in the research fund for coal and steel: European Commission. *Report, SSAB, Sweden*, August 2007.

36. Bräutigam-Matus K, Altamirano G, Salinas-Rodriguez A, et al. Experimental determination of continuous cooling transformation (CCT) diagrams for dual-phase steels from the intercritical temperature range. *Metals* 2018; 8(9): 674–689.

37. Andrews K. Empirical formulae for the calculation of some transformation temperatures. *J Iron Steel Inst* 1965; 203(7): 721–727.

38. Trzaska J. Calculation of critical temperatures by empirical formulae. *Arch Metall Mater* 2016; 61(2B): 981–986.

39. Bergweiler G. *Lokale warmebehandlung mit laserstrahlung zur verbesserung der umform- und funktionseigenschaften von hochgesten stahlen*. PhD Thesis, Faculty of Mechanical Engineering of the Rheinisch Westfalische Technische Hochschule Aachen, Germany, 2013.

Appendix I

Notation

c_p	Specific heat capacity
d_p	Sheet thickness
m	Sample mass
$\dot{q}_{cond.}$	Heat flux density through conduction
$\dot{q}_{rad.\ conv.}$	Heat flux density through radiation and convection
AA	Artificial ageing
CHD	Continuous heating dissolution
CCT	Continuous cooling diagrams
DSC	Differential scanning calorimetry
F_A	Fracture area
HAZ	Heat-affected zone
HSS	High-strength steels
LHT	Laser heat treatment
L_w	Laser beam width
$\dot{Q}_{baseline}$	Baseline heat flow
$\dot{Q}_{cond.}$	Heat flux through conduction
$\dot{Q}_{rad.\ conv.}$	Heat flux through radiation and convection
$\dot{Q}_{sample}$	Sample heat flow
RT	Room temperature
S_L	Length of sheet
SST	Solution-treated
$THTB$	Tailor heat treated blanks
UTS	Ultimate tensile strength
WQ	Water quenching
$\%EL.$	Elongation at fracture
α	Natural convection coefficient
β	Scan rate
λ	Thermal conductivity
ρ	Density